Inference of the High-Level Interaction Topology between the Metabolic and Cell-Cycle Oscillators from Single-Cell Dynamics

Ozsezen, Serdar; Papagiannakis, Alexandros; Chen, Haoqi; Niebel, Bastian; Milias-Argeitis, Andreas; Heinemann, Matthias

Published in:
Cell systems

DOI:
10.1016/j.cels.2019.09.003

Publication date:
2019

Inference of the high-level interaction topology between the metabolic and cell cycle oscillators from single-cell dynamics

Serdar Özsezen[+], Alexandros Papagiannakis[+], Haoqi Chen, Bastian Niebel, Andreas Milias-Argeitis, Matthias Heinemann*

Molecular Systems Biology, Groningen Biomolecular Sciences and Biotechnology Institute, University of Groningen, Nijenborgh 4, 9747 AG Groningen, The Netherlands

[+] These authors contributed equally

* Lead Contact: Phone: +31 50 363 8146, Twitter: @HeinemannLab, E-mail: m.heinemann@rug.nl

Summary

Recent evidence suggests that the eukaryotic metabolism is an autonomous oscillator. Together with oscillating elements of the cyclin/CDK machinery, this oscillator might form a coupled oscillator system, from which cell cycle control emerges. The topology of interactions between the metabolic oscillator and the elements of the cyclin/CDK machinery, however, remains unknown. Using single-cell metabolic and cell cycle dynamics in yeast, and solving an inverse problem with a system of Kuramoto oscillators, we inferred how the metabolic oscillator interacts with the cyclin/CDK machinery. The identified and experimentally validated interaction topology shows that early and late cell cycle are independently driven by metabolism. While in this topology S phase is coordinated by START, we obtained no support for an interaction between early and late cell cycle. The identified high-level interaction topology will guide future efforts to discover the molecular links between metabolism and the cell cycle.

Introduction

The eukaryotic cell division cycle requires the coordination of metabolically demanding processes, such as protein, membrane and cell wall synthesis, DNA replication, and the segregation of the copied material into two new cells. According to the prevalent notion, the cell cycle is driven by the self-sustained periodic activity of the cyclin/CDK machinery (Barik et al., 2010; Coudreuse and Nurse, 2010; Tyson and Novak, 2008). However, the late advent of CDKs in the evolution of eukaryotes (Krylov et al., 2003), the autonomous oscillations of late cell cycle components in non-dividing cells (Lu and Cross, 2010; Orlando et al., 2008; Slavov et al., 2011), the DNA endo-replication cycles in cell cycle arrested cells (Papagiannakis et al., 2017a; Wäsch and Cross, 2002), and the ability of cells to divide even when all early cyclins are absent (Sherr, 2004), suggest the existence of additional cell cycle control, external to

the cyclin/CDK machinery. One possibility for such external cell cycle control could be a transcriptional oscillator (Orlando et al., 2008).

Alternatively, external cell cycle control could be exerted by the recently discovered autonomous metabolic oscillator (Baumgartner et al., 2018; Papagiannakis et al., 2017a; Slavov et al., 2011). This oscillator adjusts its frequency to the available nutrients, and orbits in synchrony with the cell cycle as well as in non-dividing cells (Papagiannakis et al., 2017a). Furthermore, we have previously shown that the early (START and the early S phase) and the late cell cycle events (mitotic exit) are gated at specific metabolic phases, even during dynamic metabolic perturbations (Papagiannakis et al., 2017a). Accordingly, we suggested that metabolism and the early and late cell cycle form a system of coupled oscillators, where the coordination between cell growth and division, and thus the cell cycle, emerges as a higher-order function from the collective synchrony in the system. To understand how such synchrony is established and maintained, it is now crucial to unravel the high-level interactions between the metabolic and cell cycle oscillators.

Kuramoto models provide a simple mathematical structure to study the synchronization in systems of coupled phase oscillators (Kuramoto, 1984). Such models have been used to describe collective oscillatory behavior in biology, such as the unisonal firing of the heart-pacemaker cells and the concurrent flashing of fireflies or oscillating neural networks (Acebrón et al., 2005; Arenas et al., 2008; Hong et al., 2016; Strogatz, 2000). In Kuramoto models, the rate of phase displacement of an individual oscillator is a sum of its natural frequency and an interaction term. This term describes the interaction between each oscillator and the remaining ones through a weighted sum of the sine of the phase differences between the oscillators. Essentially, the behavior of each oscillator is determined by the interplay of its natural frequency and the interaction term. When the coupling between oscillators is sufficiently strong, and the oscillators achieve a common frequency, called compromise frequency (ω_{comp}), then they oscillate with constant phase differences between the individual oscillators. Notably, different Kuramoto model variants exists, for instance with symmetric or asymmetric coupling between the oscillators (Arenas et al., 2008; Blanter et al., 2016; Dörfler and Bullo, 2011; Tirabassi et al., 2015).

Here, using single-cell metabolic and cell cycle dynamics from different experimental conditions (Papagiannakis et al., 2017a), and a Kuramoto model, where the interactions depend solely on the phase difference between each pair of oscillators, we inferred the interactions between metabolism and three putative cell cycle oscillators (START, early S phase and mitotic exit) (Fig. 1A), corresponding to three oscillatory modules suggested earlier (Lu and Cross, 2010). We inferred the topology and strength of interactions between the oscillators by solving nonlinear optimization problems. We found that the metabolic oscillator is separately coupled to the early cell cycle (START) and the late cell cycle (mitotic

exit). While early S phase is influenced by START, there is no connection between early S and mitotic exit. Dynamic simulations of the identified model reproduced the experimentally determined metabolic frequency threshold required for cell division, as well as the dynamic behavior of the system upon nutrient shifts. Through dynamic protein depletion experiments, we further validated the identified interaction topology. The identified topology will be a crucial guide of future efforts towards unraveling the molecular connections within this system of coupled oscillators.

Results

Model and experimental data

For N coupled phase oscillators, the generic form of the Kuramoto model with asymmetric coupling is given by

$$\frac{d\theta_i}{dt} = \omega_i - \sum_{j\neq i}^{N} K_{j,i} sin\big(\theta_i - \theta_j\big), \mathrm{i} = 1, \dots, \mathrm{N} \qquad 1$$

where θ_i and ω_i are the phase and the natural frequency of the i^{th} oscillator, respectively. θ_j is the phase of j^{th} oscillator and $K_{j,i}$ is the coupling constant between the i^{th} and j^{th} oscillators, which measures the directed influence of the j^{th} to the i^{th} oscillator. The left-hand side of the equation represents the instantaneous rate of phase displacement (frequency) of the coupled oscillators. When the system is synchronized, this value is the same for all oscillators and is known as the compromise frequency ($\frac{d\theta_i}{dt} = \omega_{comp}$). The right-hand side contains the natural frequency of the oscillator, which is the frequency that it oscillates with when it is not coupled, and a term that describes the interaction between this and the other oscillators in the system.

In our experimental setup, the auto-fluorescence of the reduced nicotinamide adenine di-nucleotides NADH and NADPH was used as a reporter of the oscillating metabolism in single yeast cells (Fig. 1B). The localization of Whi5, an inhibitor of G1/S transcription, was used as a cell cycle reporter (Costanzo et al., 2004). Whi5 leaving the nucleus marks the START of the cycle commitment. Whi5 re-entering the nucleus, just before cell division, marks mitotic exit (Fig. 1C-E). Finally, the appearance of a bud on the surface of the mother cell marks the early S phase and the onset of DNA replication (Ball et al., 2011; Cvrcková and Nasmyth, 1993).

In normally dividing cells, the metabolic and the three putative cell cycle oscillators (START, early S phase and mitotic exit) synchronize at a common compromise frequency, which corresponds to the frequency of the NAD(P)H oscillations (Fig. 1B-C). The phase difference between the metabolic and the cell cycle oscillators was determined as the relative time difference of the cell cycle events from the

troughs of the metabolic oscillations (Fig. 1F and G; data from Papagiannakis et al., 2017a) and directional statistics were used to estimate the means and standard deviations of the experimentally measured phase differences (see Methods). To obtain a sufficient amount information for reverse-engineering the system, we used data from five different growth conditions (10 gL^{-1} glucose, 20 gL^{-1} galactose, 0.05 gL^{-1} glucose, 0.025 gL^{-1} glucose, 20 gL^{-1} pyruvate), each giving rise to a different natural metabolic and compromise frequencies, and phase differences. The natural frequency of the metabolic oscillator was determined in G1-arrested cells after the addition of the mating pheromone α-factor (Fig. 1H and I), which is known to halt the cyclin/CDK machinery (Bardwell, 2004).

With these experimental data (Fig. 2A), we aimed to estimate the natural frequencies of the cell cycle oscillators as well as the strength of the couplings in a Kuramoto model. The estimation of the model parameters was carried out in four steps: First, to avoid over-fitting the model, we set up a regularized optimization problem and estimated the regularization parameter (Fig. 2B). Second, using this regularization parameter, we performed a regression (Fig. 2C). Third, we performed a second regression where we introduced additional stability constraints to ensure the asymptotic stability of the synchronized solutions (Fig. 2D). Fourth, using parameter sets from the second regression round, we validated the best-fitting parameter set by generating model predictions (Fig. 2E), which we compared with novel experimental data.

Interaction topologies and natural frequencies estimated from experimental data

To estimate the coupling constants and the natural cell cycle frequencies of the Kuramoto model (Eq. 1) that best describes the experimentally observed behavior of the system, we formulated a nonlinear optimization problem. This nonlinear optimization minimized the squared distance between measured and predicted phase differences and frequencies, normalized by the standard errors of the experimental data. Given the noise of the experimental data, to prevent over-fitting and to favor sparser interaction topologies, we added a regularization term to the objective function, equal to the sum of the coupling constants weighted by the regularization parameter α, overall resulting in the following formulation:

$$\underset{\widetilde{\omega}_{comp,c},\widetilde{\omega}_{MET,c},\widetilde{\theta}_{i_c},K_{j,i},\omega_{i_{(i\neq MET)}}}{minimize} \sum_c \left(\frac{\omega^m_{comp,c}-\widetilde{\omega}_{comp,c}}{\sigma^m_{\omega_{comp,c}}}\right)^2 + \sum_c \left(\frac{\omega^m_{MET,c}-\widetilde{\omega}_{MET,c}}{\sigma^m_{\omega_{MET,c}}}\right)^2 + \sum_c \sum_{i,i\neq MET} \left(\frac{\theta^m_{i_c}-\widetilde{\theta}_{i_c}}{\sigma^m_{\theta_{i_c}}}\right)^2 +$$

$$\alpha \sum_{i,j\neq i} K_{j,i}$$

$$subject\ to \qquad (2)$$

$$\widetilde{\omega}_{comp,c} = \widetilde{\omega}_{MET,c} - \sum_{j\neq MET} K_{j,MET} \sin\left(\widetilde{\theta}_{MET_c} - \widetilde{\theta}_{j_c}\right)$$

$$\widetilde{\omega}_{comp,c} = \omega_{i_{(i\neq MET)}} - \sum_{i\neq j, i\neq MET} K_{j,i} \sin\left(\widetilde{\theta}_{i_c} - \widetilde{\theta}_{j_c}\right)$$

$$K_{j,i}, \omega_{i_{(i\neq MET)}} \geq 0$$

The subscript c denotes the growth conditions (10 gL^{-1} glucose, 20 gL^{-1} galactose, 0.05 gL^{-1} glucose, 0.025 gL^{-1} glucose, 20 gL^{-1} pyruvate), $\omega_{comp,c}$ is the compromise frequency (rad/h), $\omega_{MET,c}$ is the natural frequency (rad/h) of the metabolic oscillator, θ_{i_c} and θ_{j_c} the phases (rad) for i^{th} and j^{th} oscillators measured relative to metabolism, and $\sigma^m_{\omega_{comp,c}}$, $\sigma^m_{\omega\ MET,c}$ and $\sigma^m_{\theta_{i_c}}$ are the standard deviations of the experimentally determined variables. $K_{j,i}$ is the asymmetric coupling constant, directed from the j^{th} towards the i^{th} oscillator, and ω_i is the natural frequency of the i^{th} cell cycle oscillator (START, early S or M exit). Phases and frequencies under the tilde sign indicate quantities to be estimated (constraints for these estimates are presented in Table S1) and terms with superscript *m* indicate experimentally measured quantities. We assumed that the natural frequencies of the cell cycle oscillators START, early S and M exit are condition-independent, and thus are constant across the different nutrients.

In this non-convex optimization problem, finding the global optimum is not guaranteed. To tackle this problem, we used a multistart approach, where we started the optimizations from many different initial parameter guesses, sampled from a broad log-uniform distribution (see Table S2 for sampling ranges), using a local optimizer (CONOPT solver implemented in GAMS). To estimate the regularization parameter α, we used the L-curve method (see Methods, Estimation of the regularization parameter), where we selected the regularization parameter from the elbow of the L-curve, i.e. a point that represents the optimal compromise between fit quality and regularization. We found that this regularization parameter is equal to 0.01 (Fig. S2).

Using this regularization parameter, we then estimated the parameters of the model, using 10000 multistart optimization runs to sufficiently sample the local minima of the objective function. After removing duplicate solutions, and after excluding parameter sets leading to the trivial zero solution, we obtained 249 unique parameter sets from the 10000 multistarts (Fig. 3A). When we tested whether these parameter sets lead to stable synchronized solutions by checking the eigenvalues of the Jacobian matrix of the linearized Kuramoto system (see Methods, Derivation of a constraint for estimating parameter sets that yield stable solutions), we found that solutions with a low WSS (weighted sum of squares) tended to be stable under more conditions compared to parameter sets with high WSS (Fig. 3A). We found that maximally four conditions were stable, with the pyruvate condition most often being unstable. Because of the uncertainty in the experimental data (measurement noise and cell-to-cell variability) and the complex landscape of the objective function, we not only considered the optimization run with the lowest WSS, but retained all well-fitting parameter sets with WSS $\leq$ 2.56 (corresponding to approximately two times of the minimum WSS), amounting to in total 17 unique parameter sets below this threshold (Fig. 3A).

Across these 17 parameter sets, we found that some parameters had rather broad distributions (Fig. 3B). $K_{START,S}$ had the highest median value, followed by $K_{M,START}$ and $K_{MET,M}$. ω_{START} was the highest natural frequency, while ω_M was practically zero (Fig. 3B). Looking at the topologies of the 17 parameters sets in a binary fashion, i.e. only considering the presence (value greater than zero) or absence (zero) of a coupling constant, we found two types of connection patterns: Z-like topologies (Fig. S3A), where $K_{MET,M}$, $K_{M,START}$ and $K_{START,S}$ are commonly represented, and C-like topologies (Fig. S3B), which all contain $K_{MET,M}$, $K_{MET,START}$ and $K_{START,S}$. Among the 17 parameter sets, we found one Z- and one C-topology that are stable on four nutrient conditions except pyruvate (Fig. S3).

Towards obtaining parameter sets that are stable under all five conditions, we re-ran the optimization, now with an additional constraint, which enforces local asymptotic stability of the synchronized solutions. Specifically, we added the Routh-Hurwitz stability criterion (Franklin et al., 1993) for the linearized system as an additional constraint to the optimization problem (see Methods, Derivation of a constraint for estimating parameter sets that yield stable solutions). As this stability constraint introduces three additional nonlinear inequalities, it increases the difficulty of the optimization. For this reason, we only implemented this constraint for the two extreme conditions, i.e. 10 gL^{-1} glucose and 20 gL^{-1} pyruvate (corresponding to the highest and lowest natural metabolic frequency, respectively), with the expectation that once the extreme conditions are stable, there is a good chance that rest of the three conditions would also be stable as well.

Out of the 10000 multistart optimizations, 3495 finished successfully, generating 954 unique parameter sets. Out of these, 48 were able to achieve a stable steady state at all five nutrient conditions (i.e. fulfilling the Routh-Hurwitz stability criterion for all five conditions), although as mentioned only the two extreme conditions were required to be stable in the optimization. Similar to the analysis of the first optimization round, we set a threshold for WSS (WSS $\leq$ 3), below which there were 18 unique parameter sets able to achieve steady-state under all five conditions (Fig. S4A). The best fit from these 18 parameter sets had a WSS of 2.19, and fitted the experimental data well without systematic deviation (Fig. 3C).

The distributions of the parameters across these 18 parameter sets (Fig. 3D) were considerably narrower compared to the ones from the first optimization round without the stability constraints (Fig. 3B). $K_{MET,START}$ had the highest median value, followed by $K_{MET,M}$ and $K_{START,S}$. The 18 unique parameter sets belong to 8 unique binary topologies (Fig. S4B). All topologies contained the couplings $K_{MET,M}$ and $K_{START,S}$, and 7 out of 8 also contained $K_{MET,START}$, giving rise to the C-like topology. Because these three coupling constants are present in all stable topologies and have relatively higher values, this indicated that these directional couplings are essential to achieve steady state behavior close to experimentally measured values.

Integrating the information obtained from these 18 parameter sets, we derived an interaction topology as shown in Fig. 3E. Here, it is important to note that despite potentially existing identifiability issues, we found that our numerical workflow is robust, as (i) the magnitude differences between the identified parameters are preserved with the introduction of noise into the data (Fig. S5A, B), (ii) we could recover the correct interaction topology when solving the inverse problem with a known solution using noisy simulated data (Fig. S5C, D), and (iii) the results could also be generated with an alternative optimization solver (Fig. S5E).

In the derived topology, the metabolic oscillator separately controls START and the late cell cycle (Mitotic exit). Further, the natural frequency of M exit is almost zero (Fig. 3D), which suggests that the late cell cycle is not an oscillator, but that it is dragged along by the metabolic oscillator through the strong coupling. In contrast, the natural frequencies of the early cell cycle oscillators (START, early S) are higher than the condition-dependent natural metabolic frequencies. As metabolism has a strong effect on START ($K_{MET,START}$), which is further propagated to the early S oscillator (via $K_{START,S}$), this means that the metabolic oscillator slows down the early cell cycle upon coupling.

Model predictions and experimental validation

The Routh-Hurwitz stability criterion ensures local asymptotic stability (Franklin et al., 1993) but does not specify the range of perturbations over which the system will return to steady-state. To test the stability and robustness of the model, we integrated the ODEs with different initial conditions around the synchronized solution, using the best fitting parameter set. Here, we found that the system moves back to the same steady state (Fig. 4A), demonstrating that the identified model robustly yields a stable system behavior.

Next, we checked whether synchrony is maintained also when the natural metabolic frequency is changed dynamically. Therefore, we integrated the ODEs starting from the metabolic frequency and phase differences corresponding to the 0.025 gL^{-1} glucose condition (low glucose), and over six simulation hours gradually changed the metabolic frequency to the one in 10 gL^{-1} glucose (high glucose). Here, we observed that the system could adjust without losing synchrony, reaching the experimentally observed compromise frequency and phase differences in high glucose (Fig. 4B). This was possible also with the rest of the parameter sets (Fig. S6A,B). Also, a slow shift in the reverse direction (from high to low glucose) was possible for all parameter sets (Fig. S6). Thus, the model is also stable during gradual dynamic changes of the metabolic frequency. When we simulated the system with metabolic frequencies lower than of 20 gL^{-1} pyruvate, however, we observed that synchrony was lost for all 18 parameter sets (Fig. 4C, Fig. S7). This simulation result is consistent with our previous experimental observation, where

cells with a natural metabolic frequency below 0.15 h^{-1} (0.94 rad/h) fail to commence their cell division program (Papagiannakis et al., 2017a).

Next, we tested step-changes in the natural metabolic frequencies. First, we integrated the ODEs starting from a metabolic frequency and phases corresponding to low glucose (0.025 gL^{-1} glucose) and switched suddenly to a metabolic frequency corresponding to high glucose (10 gL^{-1} glucose). Here, all 17 parameter sets accomplished the sudden glucose upshift (Fig. 5A, Fig. S8). In contrast, only three parameter sets accomplished synchrony with phase differences close to the estimated ones after the sudden nutrient downshift (Fig. 5A, and Fig. S8 for details). We validated these predictions qualitatively in microfluidics experiments. Here, before and after the nutrient shifts, we observed the occurrences of Start, budding/early S and Mitotic exit and cytokinesis (Fig. 5B). As a measure for adaptation and synchrony maintenance in the system we used the budding rate after the perturbation (glucose upshift or downshift) compared to the budding rate at steady state (on high or low glucose, respectively). If the budding rate after the perturbation is similar to the budding rate during steady state growth on the same glucose condition, this means that the system adapts and synchrony is maintained. Here, we found that after the glucose upshift, cells budded at a budding rate similar to the rate on steady-state high glucose growth. Conversely, after the glucose downshift, cells produced significantly less buds compared to the steady-state low glucose growth (Fig. 5C), which indicates a loss of synchrony, in line with the model prediction. Similar conclusion were drawn when performing the analysis on the basis of cytokinesis (Fig. 5D).

As the inferred interaction topology suggests that early and late cell cycle are separately influenced by the metabolic oscillator (Fig. 3E), we conjectured that a removal of the mitotic exit should still lead to synchrony of the residual oscillators. To test this conjecture, we simulated the system for all 18 parameter sets by setting the coupling constants related to mitotic exit to zero ($K_{i,M}, K_{M,i} = 0 \; \forall \; i \in \{MET, START, S\}$). Here, simulations with 12 out of 18 parameter sets yielded stable phase differences (Fig. 6A) and achieved synchrony. This simulated behavior is in line with our previous experimental observation: when we perturbed mitotic exit by dynamically depleting Cdc14 using the yeast-adapted auxin-inducible degron (AID) (Morawska and Ulrich, 2013; Nishimura et al., 2009; Papagiannakis et al., 2017b), NAD(P)H oscillations persisted in synchrony with waves in cell size increase (biomass synthesis) and genome replication (i.e. S phase) (Papagiannakis et al., 2017a). As an increased biomass synthesis including protein production has been linked to START (Polymenis and Aramayo, 2015), biomass synthesis can serve as a dynamic proxy for the START oscillator. The simulation with decoupled mitotic exit further predicted a slightly faster compromise frequency compared to the complete model topology. The predicted compromise frequencies of the complete and the reduced topologies fall within the 25th

and 75th percentile of our experimentally measured compromise frequencies before and after Cdc14 depletion (Fig. 6B).

Next, we stripped down the system even further by removing both mitotic exit and the S phase. Here, we found that the remaining system had a compromise frequency, similar to the full system and it remained coupled for 7 out of 18 parameter sets with similar phase differences as the unperturbed system (Fig. 6C). Towards validating this prediction, we targeted Cdc20 for auxin-inducible degradation. Cdc20 regulates mitotic exit by promoting the release of Cdc14, as well as the separation of sister chromatids (Shirayama et al., 1999; Wäsch and Cross, 2002). When Cdc20 is depleted, cells do not complete mitosis, and they cannot begin new rounds of DNA replication (Shirayama et al., 1998). Consistently, when we depleted Cdc20 many cells were unable to divide and maintained a 2N chromosomal content. However, in some cells metabolic oscillations persisted (Fig. 6D) with normal frequencies in the hour range, in synchrony with biomass waves (Fig. 6F), but in absence of genome replication (Fig. 6G, H) and mitotic exit (Fig. 6E, H), in line with the model predictions.

Discussion

Using single cell microscopy data, i.e. metabolic and cell cycle dynamics from cells grown on multiple nutrient conditions, we inferred an abstract interaction topology between the metabolic oscillator and three oscillatory cell cycle modules, which were proposed earlier (Lu and Cross, 2010). The reconstructed Kuramoto model with non-symmetrical coupling constants is able to describe the synchronous dynamics of metabolism and cell cycle. In the identified coupled oscillator system, the early cell cycle (START and S phase) and late cell cycle (mitotic exit) are separately orchestrated by the metabolic oscillator, and no significant link between the early and late cell cycle could be identified (Fig. 3E for details, Fig. 7 for a more visual impression of the envisioned functioned of the inferred system). Simulation results upon dynamic and structural perturbations of the system corresponded to respective experimental perturbations, including dynamic protein depletion experiments with cell cycle proteins (i.e. Cdc14 and Cdc20).

Inferring features of oscillator systems with dynamic models is challenging, as this requires exploration of a high-dimensional parameter space with multiple local optima, which may correspond to unstable systems of oscillators (Pitt and Banga, 2019). Most approaches proposed so far for the reconstruction of interactions between coupled Kuramoto oscillators have been based on the assumption that the time evolution of the phase of each node can be followed over time. Based on the continuous observations of the node phase dynamics, various statistical measures can be calculated for pairs of nodes, which are ultimately used to determine the connectivity pattern of the network (Alderisio et al., 2017; Cadieu and Koepsell, 2010; Kralemann et al., 2011; Tirabassi et al., 2015). Another method relies on driving one or more nodes with small, temporally constant external input signals, and making use of the linearized

system to algebraically calculate the connectivity pattern of the network from the perturbed synchronized solutions (Timme, 2007). Given the large amount of noise present in single-cell time series and the technical challenges associated with dense time sampling of single-cell dynamics, in this work we pursued a more robust, optimization-based approach which makes use of steady-state information (averages of phase differences and compromise frequencies at synchrony) at different natural frequencies of the metabolic oscillator, and which explicitly accounts for measurement uncertainty. It should be noted that an alternative approach to the use of regularization could have been a fully Bayesian treatment of the inference problem. However, such an approach would be problematic, as the equality constraints used to define the system steady-state would make both prior construction and posterior sampling very challenging.

Assessing the structural identifiability properties of a complex dynamical system, such as the one considered here, is always a necessary step towards establishing the validity of the inference results (Villaverde and Banga, 2017). However, the regression problem treated here assumes the presence of measurement error both in the dependent and independent variables. The structural identifiability of such a nonlinear errors-in-variables model is, to the best of our knowledge, very likely impossible to assess. However, we have carried out several alternative analyses (Fig. S5), which show that the inferred topology is robustly recovered, despite the presence of mild practical identifiability issues in the model.

The inferred topology of the coupled oscillator system describes the actual molecular system on a highly abstract level. The actual system is likely much more complex, and it therefore cannot be expected that the model can capture detailed interactions. Yet, despite the fact that we considered condition-independent natural frequencies of the cell cycle oscillators, the model captures the observed condition-dependent cell cycle durations, and the observed condition-dependent phase shifts between the oscillators. Beyond, it is remarkable that our inferred topology is consistent with a number of previous findings, which were notably not used in the inference of the system. First, late cell-cycle proteins (e.g., Cdc14 and Sic1) oscillate when the cell cycle is halted, on the basis of which, it had been concluded that there are Cdc14 endocycles (Lu and Cross, 2010; Rahi et al., 2016). Second, cell-cycle entry can occur even in the absence of major cell-cycle machinery components (e.g., the early cyclins) (Sherr, 2004). Both observations could be explained by the here identified strong coupling with the metabolic oscillator. Beyond, a recent genome-scale reconstruction of the cell-cycle control network has suggested that the cell cycle control network falls apart into three distinct control circuits; G1/S, G2/M and M/G1, and highlighted that it has been difficult to find a mechanistic link between the G1/S (Cln1/2, Clb5/6 expression) and G2/M (Clb1/2 expression) transitions (Münzner et al., 2019). The here identified high-level connections from the metabolic oscillator to the cell cycle instead could fulfil a coordinating role.

A key question now is what the corresponding molecular links are for the identified high-level couplings in the system. The identified connection between metabolism and START, which is in line with a recent suggestion (Burnetti et al., 2016), could be associated with the hypothesized growth-induced dilution of Whi5 (Schmoller et al., 2015) and its nutrient dependent concentration (Liu et al., 2015), could be connected with the acetyl-CoA-dependent epigenetic activation (via histone acetylation) of CLN3 transcription (encoding an early cyclin) (Cai et al., 2011; Shi and Tu, 2013), or alternatively might be established by the differential scaling between the rate of protein synthesis and cell size dynamics in G1 that we recently found to cause increased levels of Cln3 triggering START (Litsios et al., 2019). The identified connection between START and the S phase possibly represents the transcriptional program triggered by early cyclins leading to the expression of Clb5 and Clb6 to induce genome replication (Bloom and Cross, 2007; Schwob and Nasmyth, 1993). Less is known about the identified connection from metabolism to mitotic exit. An element of this connection could be the acetyl-CoA carboxylase and the synthesis of certain lipid species, which are essential for yeast to go through the G2/M transition (Al-Feel et al., 2003). Similar observations have recently been reported recently also for mammalian cells and fission yeast (Scaglia et al., 2014; Zach et al., 2018). Lipid synthesis could be part of the biochemical processes that constitute the metabolic oscillator, signaling mitosis across eukaryotes. Although the connection between the early and late cell cycle is thought to be facilitated by a cascade of transcription factors and B-type cyclins/CDK (Cho et al., 2017; Rahi et al., 2016), we did not find a strong link between the S phase and mitotic exit, in line with the findings of the recent genome-scale reconstruction of the cell cycle control network (Münzner et al., 2019). In our system, the coordination between the early and the late cell cycle is achieved mainly via the metabolic oscillator and its connections directed to START and mitosis (M) (Fig. 7).

Overall, in this work, we have solved an inverse problem, and thereby unraveled the high-level interaction topology of the complex molecular system that coordinates cell growth and division process. Knowledge of the interaction topology of this system, where the early and late cell cycle are separately coordinated by metabolism, will guide future efforts to identify the molecular mechanisms that give rise to this coordination and synchrony.

Acknowledgments

Funding from the following sources is acknowledged: EU Commission for ITN ISOLATE (for MH and AP) and ITN MetaRNA (for MH and SÖ); Chinese Scholarship Council (for HC). AM-A would like to thank Corentin Briat for helpful discussions on the implementation of the stability constraints.

Author contributions

Conceptualization: AP, BN, MH; Software: SÖ; Formal analysis: SÖ, AP, HC; Investigation: SÖ, AP, HC, AM; Visualization: AP, SÖ, HC; Writing—original draft: AP, SÖ, MH; Writing—review and editing: AP, SÖ, HC, AM, MH; Supervision: MH; Funding acquisition: MH, HC; Project administration: MH

Declaration of Interests

The authors declare no competing interests.

Main figure titles and legends

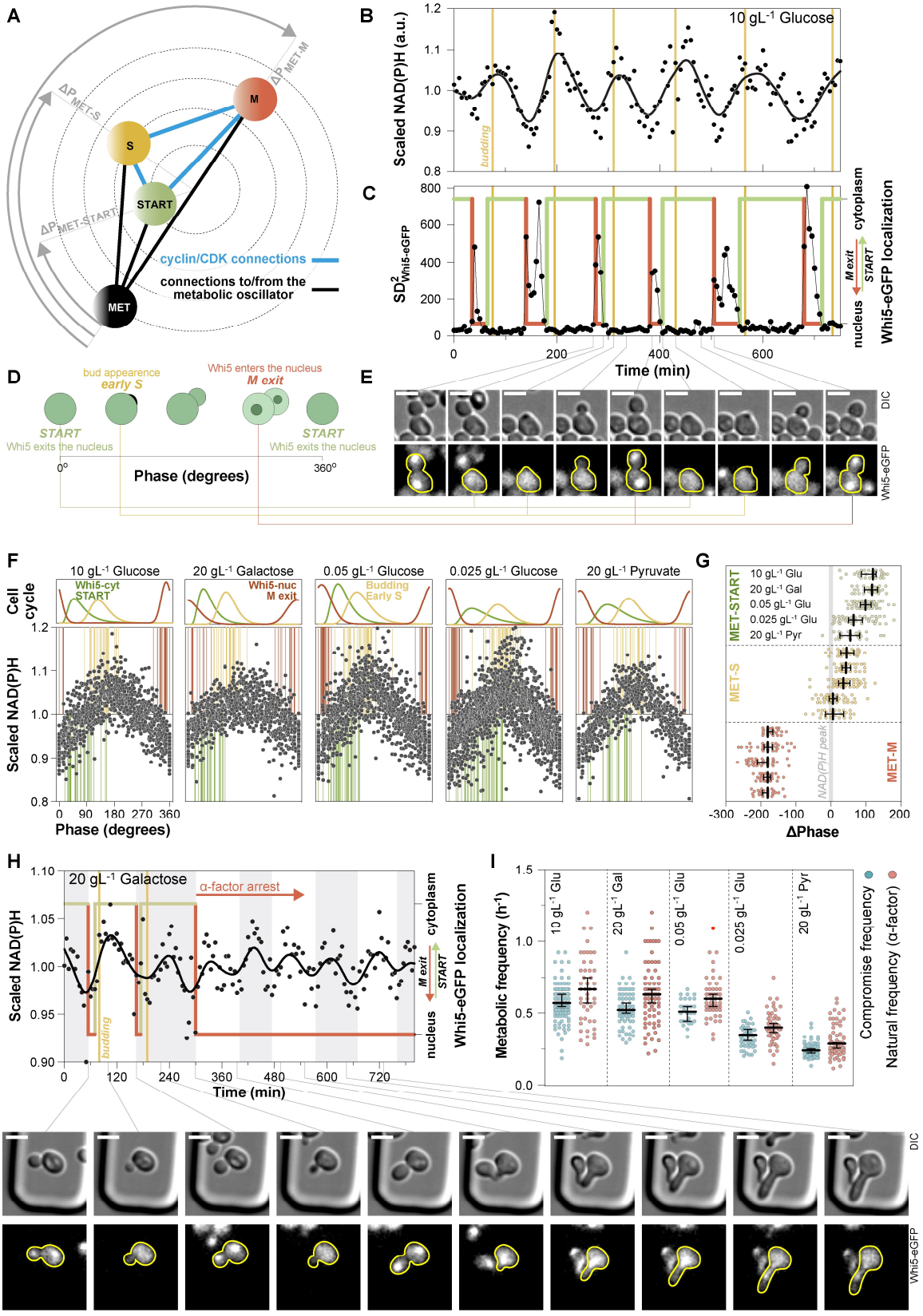

Figure 1: Experimental data reveals the synchrony between cell cycle and metabolic oscillations. (A) We derived a system of four coupled oscillators, including the autonomous metabolic oscillator (MET), the START oscillator (START), the early S phase oscillator (S) and the mitotic exit oscillator (M). We considered three cell cycle oscillators, because our earlier observations of the phase changes between the cell cycle events of START, early S and mitotic exit corresponding to different growth conditions (Papagiannakis et al., 2017a) could not be explained by the behavior of a single cell cycle oscillator. In fact, three corresponding CDK-independent oscillating cell cycle modules had been suggested before (Lu and Cross, 2010). **(B)** The NAD(P)H auto-fluorescence was used as a metabolic reporter. The frequency of metabolism when it oscillates in synchrony with the cell cycle corresponds to the compromise frequency of the system. The natural frequency of metabolism we measured in G1-arrested cells, treated with mating pheromone alpha factor (Papagiannakis et al., 2017a). Data from a single cell growing on high glucose (10 gL^{-1}) are presented. The raw NAD(P)H signal was de-trended by dividing over a fitted smoothing spline (MATLAB and Curve Fitting Toolbox, smoothing spline: p-value 1e-06) to remove low frequency noise. **(C)** Cell cycle reporters were used to determine the phase of the cell cycle oscillators relative to metabolism. The time point when Whi5, a repressor of cell cycle transcription, leaves the nucleus and enters the cytoplasm (vertical green lines) marks START. The appearance of a bud on the surface of the mother cell (vertical orange lines) reports the onset of the S phase. Mitotic exit is marked as the time when Whi5 re-enters the nucleus (red vertical lines). The Whi5-eGFP localization was determined by manual inspection (right y-axis), as it appears in Fig. 1E, and confirmed using the squared standard deviation (variance) of the Whi5-eGFP fluorescence. Data from a single cell are presented (same cell as in Fig. 1B). **(D)** Schematic representation of the Whi5 localization and budding cycles used to determine the phase of the cell cycle oscillators. **(E)** Microscopy images (scale bar: 5 μm), linked to Fig. 1B-C, display the onset of budding (DIC channel) and the Whi5-eGFP localization in the nucleus or the cytoplasm (GFP channel). Yellow outlines mark the mother cell (shown in Fig. 1B-C) and its associated bud. **(F)** The distribution of the START (green), budding/Early S (yellow) and M exit (red) on the metabolic oscillations. Metabolic oscillations were overlaid for each nutrient condition by converting time into phase between consecutive troughs in the NAD(P)H signal. Vertical lines indicate the cell cycle event: START (green), budding/Early S (yellow) and M exit (red), lognormal distributions were fitted to the phase of each cell cycle event to indicate its occurrence relative to the metabolic oscillator. **(G)** The phase differences between metabolism (MET) and the cell cycle (START, S and M exit) across nutrients (same data as in Fig. 1F). The phase difference between metabolism and the early cell cycle (START and S) is nutrient-dependent, whereas M exit always occurs at the troughs of the metabolic oscillations. The medians and their 95% CI are presented. **(H)** Metabolic oscillations measured in a single cell that was arrested in G1 (Whi5 in the nucleus) after alpha factor treatment. The raw NAD(P)H signal was de-trended by dividing over a fitted smoothing spline (MATLAB and Curve Fitting Toolbox, smoothing spline: p-value 2e-06) to remove low frequency noise. Alternating white and grey regions are used to distinguish between consecutive metabolic oscillations before as well as after cell cycle arrest. Microscopy images (scale bar: 5 μm) display budding (DIC channel), the Whi5-eGFP localization in the nucleus or the cytoplasm (GFP channel) and the 'shmoo' phenotype after alpha factor treatment (DIC channel). More metabolic oscillations in alpha factor arrested cells are presented in Fig. S1A. **(I)** The compromise metabolic frequencies (in synchrony with the cell cycle – blue markers) and natural metabolic frequencies (in G1 arrested cells – red markers). The medians and their 95% CI are presented. The alpha factor mediated cell cycle arrest results to natural metabolic frequencies similar to those in cells spontaneously skipping cell cycle (Fig. S1B-D). See also Figure S1.

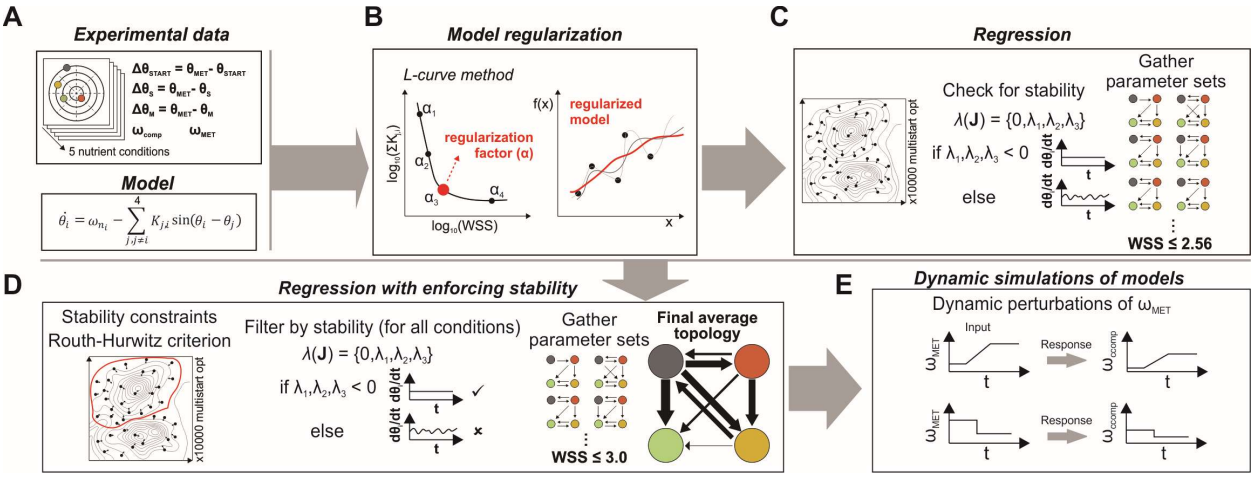

Figure 2: Model identification procedure. (A) To estimate the model parameters (natural frequencies of the cell cycle oscillators and coupling constants), we fitted the Kuramoto model with asymmetric coupling constants to the experimental data (compromise frequencies, natural frequencies of metabolism and phase differences between the oscillators) from five different nutrient conditions (10 gL^{-1} glucose, 20 gL^{-1} galactose, 0.05 gL^{-1} glucose, 0.025 gL^{-1} glucose, 20 gL^{-1} pyruvate). **(B)** To avoid over-fitting, we added a regularization term to the objective function. The regularization parameter was estimated with the L-curve method. **(C)** We solved the unconstrained regularized nonlinear optimization problem with multi-starts and checked the stability of the identified systems. The eigenvalues of the Jacobian matrices at all five conditions were calculated as a stability measure. **(D)** To identify parameter sets that are stable at all five conditions, we enforced stability using the Routh-Hurwitz criterion as a constraint in the regularized nonlinear optimization problem, which we again solved with multi-starts. **(E)** Finally, we checked the stability of the identified models with dynamic simulations. See also Figure S2.

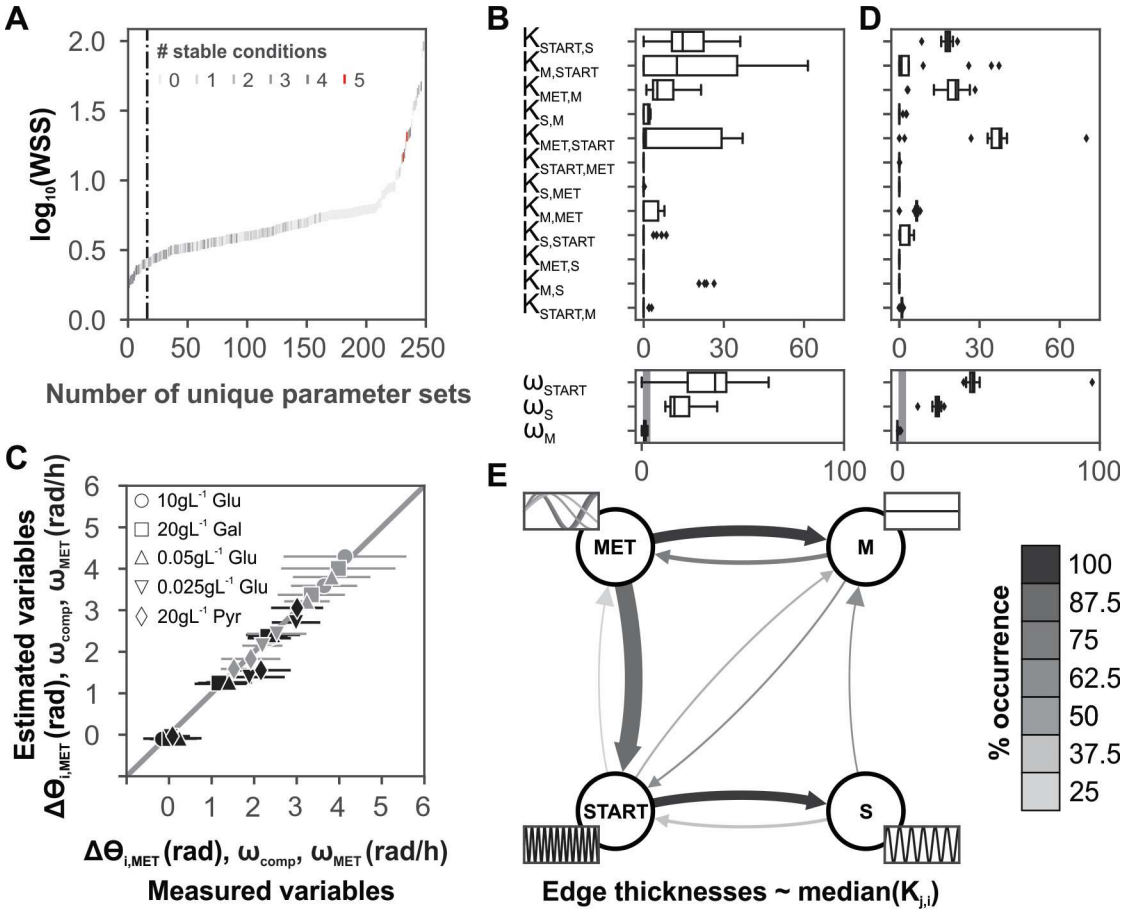

411

412 **Figure 3: Regression results and estimated interaction topology. (A)** The weighted sum of squares (i.e. distance from
413 experimental data) in log10 scale of the unique parameter sets obtained from 10000 multistart optimizations (unconstrained). The
414 parameter sets were sorted by the increasing $\log_{10}$(WSS), or from the best to the worst fit, from left to right, different scales of
415 grey indicate the number of nutrient conditions the parameter sets yield stable dynamics. Color gets darker as the number of
416 stable conditions increases. For a given parameter set and nutrient condition, if eigenvalues are less than or equal to zero, the
417 system is considered to be stable at that nutrient condition (see Methods, Derivation of a constraint for estimating parameter sets
418 that yield stable solutions). Red ones indicate the parameter sets where all coupling constants are zero. The dashed line indicates
419 the threshold we selected as a filter for analyzing relatively good fitting parameter sets (WSS ≤ 2.56). **(B)** Distributions of the
420 coupling constants (top) and the natural frequencies (bottom) from first regression round (with 17 unique parameter sets). In the
421 frequencies plot (bottom), the shaded area indicates the range of the natural metabolic frequencies from 10 gL^{-1} glucose (fastest)
422 to 20 gL^{-1} pyruvate (slowest). **(C)** Measured phase differences and frequencies against best fitting parameter set from the second
423 regression round (WSS = 2.19). Black markers indicate the phase differences and grey markers indicate the compromise and
424 metabolic frequencies under different nutrient conditions. Horizontal lines indicate the standard deviation of the experimental
425 measurement. **(D)** Distributions of the coupling constants (top) and the natural frequencies (bottom) from second regression
426 round with stability constraints (includes 18 unique parameter sets). **(E)** Common edges (directional coupling constants) in
427 parameter sets found in the second optimization round. The thickness of the arrows is proportional to medians of coupling
428 constants values (shown in Fig. 3D). The grey scale of the arrows corresponds to the representation of the edges in the parameter
429 sets. The median natural frequencies of the cell cycle are represented as waveforms for each node. Similarly, the measured mean
430 metabolic frequencies for each nutrient condition are shown. Faster metabolic waves (e.g. in 10 gL^{-1} glucose) are darker than the

ones with low frequency (e.g. 20 gL^{-1} pyruvate) which are lighter grey. All natural waveforms are plotted within a two-hour time period (i.e. sin $(\omega_i t)$). See also Figure S3, S4 and S5.

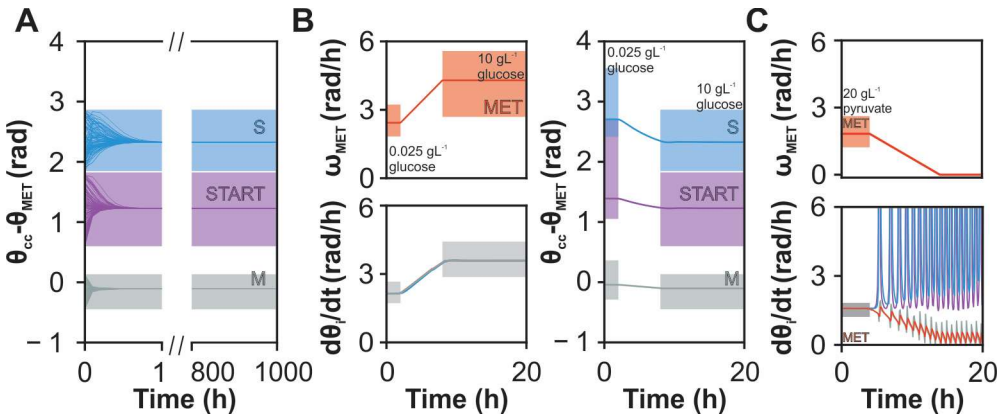

Figure 4: The identified system is stable when simulated and perturbed dynamically. (A) Phase angle trajectories of cell cycle elements (at 10 gL^{-1} glucose condition) with respect to metabolism for the best fitting parameter set. We integrated the system of ODEs 100 times for 1000 simulation hours, sampling initial phase values within the standard deviation of the experimental measurements (shaded areas: $\theta_{i_c}^m \pm \sigma_{\theta_{i_c}}^m$). **(B)** Simulation results for dynamically changing the natural metabolic frequency from 0.025 gL^{-1} glucose to 10 gL^{-1} glucose condition within 6 simulation hours. Upper left plot shows the input metabolic frequency (shaded area: $\omega_{MET,c}^m \pm \sigma_{\omega\ MET,c}^m$). Lower left plot shows the frequencies of the coupled oscillators in synchrony (shaded area: $\omega_{comp,c}^m \pm \sigma_{\omega_{comp,c}}^m$). At steady state all the oscillators compromise at the same frequency. Right plot shows the phase angles of the cell cycle oscillators with respect to metabolism (shaded areas: $\theta_{i_c}^m \pm \sigma_{\theta_{i_c}}^m$). **(C)** Natural metabolic frequency (top) and individual frequencies of oscillators (bottom) from the simulations where we slowly shifted metabolic frequency from 20 gL^{-1} pyruvate condition to zero using the best fitting parameter set (shaded area: $\omega_{MET,c}^m \pm \sigma_{\omega\ MET,c}^m$). In the bottom plot the frequencies of all oscillators in the system are shown. Prior the perturbation all oscillators are in synchrony at a common compromise frequency (shaded area: $\omega_{comp,c} \pm \sigma_{\omega_{comp,c}}^m$). See also Figure S6 and S7.

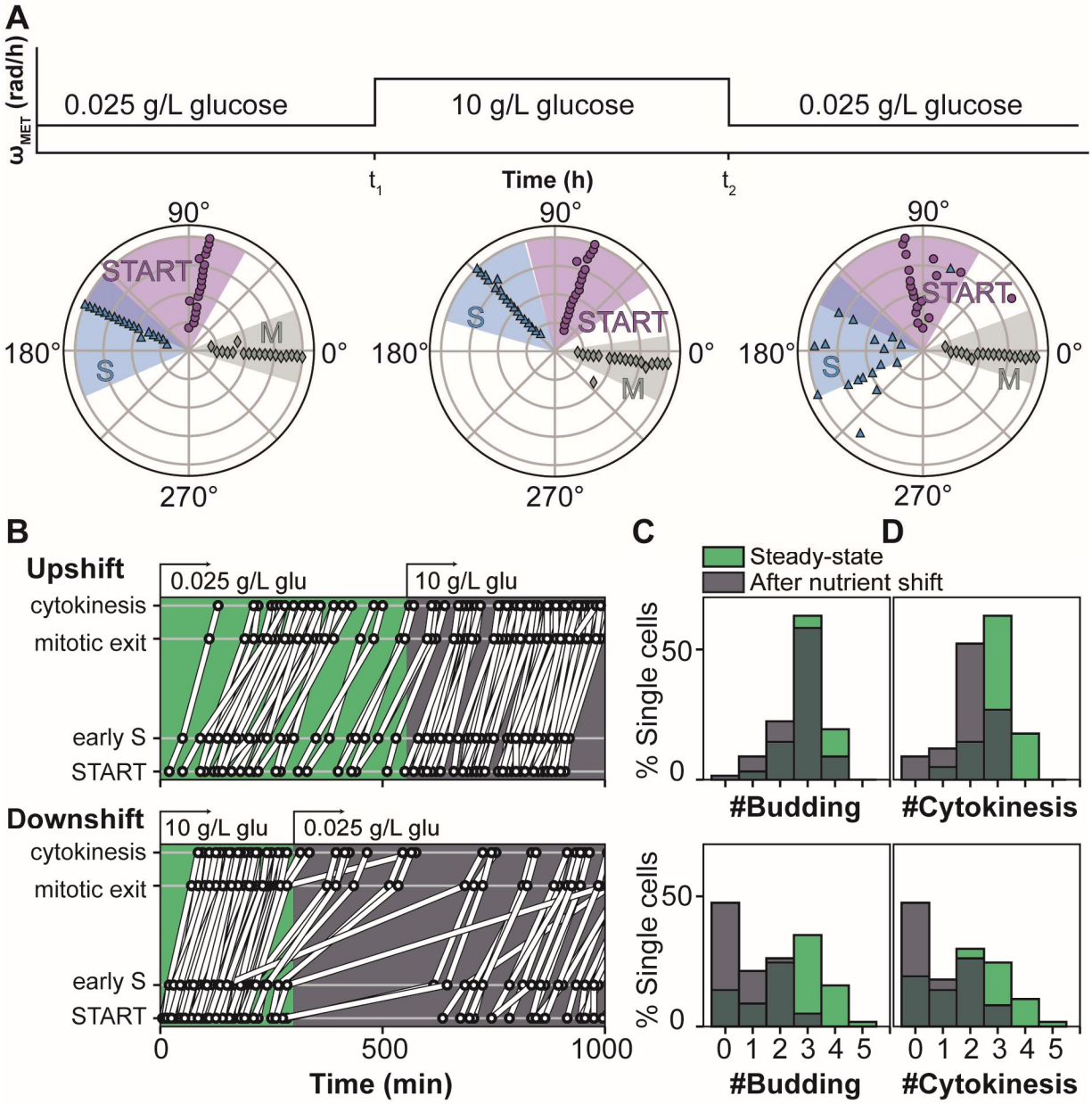

Figure 5: Nutrient shift simulations reproduce the nutrient shift experiments. (A) The phase angles of cell cycle elements relative to metabolism from simulations (model integration for 1000 simulation hours) where the natural metabolic frequency was changed from the corresponding frequency on low glucose to the one on high glucose (step-change at t_1 = 500 h), or in reverse from high to low glucose (step-change at t_2 = 500 h). Two distinct simulations were performed, one for each switch. The polar plot on the left corresponds to the cell cycle phases relative to metabolism 500 h before the nutrient upshift (t_1). The middle polar plot corresponds to the cell cycle phases relative to metabolism at 500 h after the nutrient upshift (t_1). The polar plot on the right corresponds to the cell cycle phases relative to metabolism 500 h after the nutrient downshift (t_2). The shaded areas indicate the standard deviation of the experimental measurements ($\theta_{i_c}^m \pm \sigma_{\theta_{i_c}}^m$). **(B)** Cell cycle events (START, budding/early S, mitotic exit and cytokinesis) observed in an ensemble of cell cycles before and after a nutrient shift; upshift: from 0.025 gL^{-1} to 10 gL^{-1} glucose, shift was made at t = 555 min; downshift: reverse, shift was made at t = 300 min. Each white line resembles data from an individual cell cycle. Data from n = 20 single cells with active cell cycle before the shift are plotted for each experiment. **(C)**

Distribution of the number of buds produced per single cell within 300 minutes on 10 gL^{-1} glucose (top), or 700 minutes on 0.025 gL^{-1} glucose (bottom). The duration of the bud counting period is proportional to the average growth rate on each nutrient condition (see Method Details). In the top histogram, cells grown on 10 gL^{-1} glucose unperturbed (green, n = 62), or after being switched from to 0.025 gL^{-1} glucose (grey, n = 67) are presented. In the bottom histogram, cells grown on 0.025 gL^{-1} glucose unperturbed (green, n = 57), or after being switched from to 10 gL^{-1} glucose (grey, n = 61) are presented. **(D)** Similar as (C) but now showing the distribution of the number of cytokinesis events. See also Figure S8.

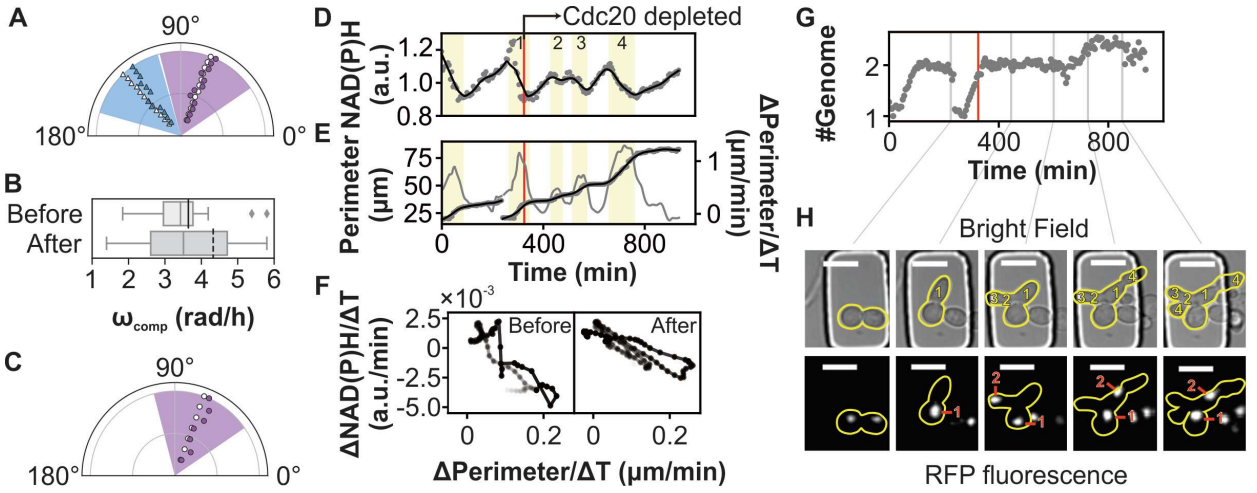

Figure 6: Cdc20 and Cdc14 dynamic depletion experiments validate the simulations of the reduced model topologies. (A) Phase angles of cell cycle elements relative to metabolism for the simulations without mitotic exit and **(C)** without mitotic exit and S. White markers show the initial values (t = 0 h, at 10 gL^{-1} glucose condition) and colored markers show the values at the end of the simulation (t = 1000 h). Purple and blue colors indicate START and early S. Shaded areas indicate the experimental measurement range for phase angles ($\theta_{i_c}^m \pm \sigma_{\theta_{i_c}}^m$). **(B)** Frequency of the system before and after Cdc14 depletion (before: n = 31; after: n = 32). Solid black line shows the mean of the measured compromise frequency ($\omega_{comp,c}^m$) on 10 gL^{-1} glucose. Dashed black line shows the median compromise frequency of the simulations that yield stable solutions (12 parameter sets as indicated on A). **(D - H)** An example cell that showed synchronized oscillations after Cdc20 depletion. The vertical red line in (D/E/G) indicates the time when Cdc20-AID was depleted (Supplementary Movie 1). **(D)** The NAD(P)H signal was de-trended by dividing by a fitted LOWESS spline. **(E)** Biomass waves of the cell indicated by its perimeter (grey markers). The cellular perimeter was smoothed (black line) and its derivative was estimated (grey line – rate of perimeter increase). Yellow shades in (D) and (E) indicate phases of fast biomass production (peaks in the perimeter increase rate – grey line). Numbers in yellow shades correspond to yellow numbers in (H). **(F)** The oscillating NAD(P)H and perimeter increase rates are coordinated before and after Cdc20 depletion. Derivatives are calculated based on fitted smoothing splines. The grayscale of data points represent the order in time (darker indicates latter in time). **(G)** Genome copy number, derived from the normalized Hta2-mRFP fluorescence (see Method Details). **(H)** Microscopy images for certain time points (as indicated by gray lines pointing to (G)) in the brightfield and RFP channels (Hta2-mRFP) show the increase in perimeter and halted genome replication. Yellow and red numbers indicate biomass waves and genome copies respectively. Scale bar: 10 μm.

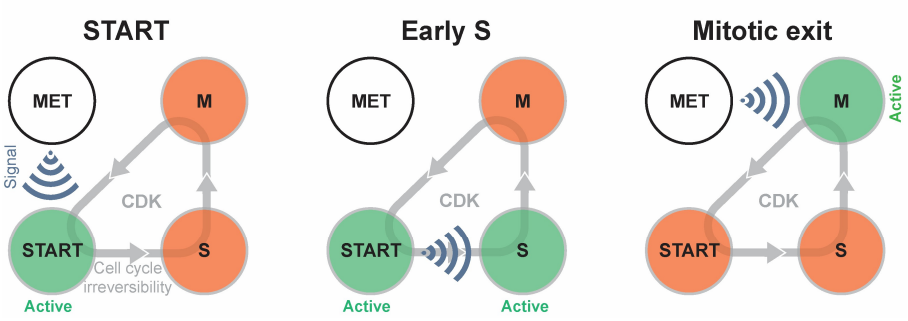

Figure 7: Overview about coupled oscillator system. The metabolic oscillator orchestrates the early cell cycle (START and S phase) and late cell cycle (mitotic exit) are separately.

STAR Methods

LEAD CONTACT AND MATERIALS AVAILABILITY

Further information and requests for resources and reagents should be directed to and will be fulfilled by the Lead Contact, Matthias Heinemann (m.heinemann@rug.nl). All materials can be freely obtained from the authors. Plasmids generated in this study have been deposited to Addgene (IDs 130269 and 130270). This study did not generate new unique reagents.

EXPERIMENTAL MODEL AND SUBJECT DETAILS

All yeast strains used are indicated in the key resources table.

METHOD DETAILS

Cell cultivation and microfluidics

To obtain exponential growing cultures on 10 gL^{-1} glucose, a single colony growing on a YPD 20 gL^{-1} glucose agar plate was used to inoculate 10 mL 10 gL^{-1} glucose minimal medium in 100 mL shake flasks, grown (at 30°C, 300 rpm) to late- or post-exponential phase (OD>2.0). The culture was then diluted to OD 0.01 and grown again to an OD between 1 and 1.5. For nutrient downshift and the steady-state high glucose microfluidic experiments, as well as the Cdc20 depletion experiments, this culture was then diluted to OD 0.05, further grown for 2 hours and used for loading of the microfluidic chips. To obtain cells exponentially growing on 0.025 gL^{-1} glucose, a post-diauxic shift culture on 10 gL^{-1} glucose (OD > 5.0) was diluted with 0.025 gL^{-1} glucose to OD 0.01, grown to OD 0.25, diluted to OD 0.02, and grown again to OD 0.05~0.1, and used for loading. Before dilution, flasks with medium were pre-warmed and aerated.

Loading of the microfluidics device was performed as previously described (Huberts et al., 2013). In the nutrient downshift and steady state low glucose experiments, as well as the Cdc20 depletion experiment, a syringe pump was used for medium perfusion (Harvard Apparatus), and medium switches were done manually by cutting and re-joining the tubes. Nutrient upshift and steady state high glucose experiments were performed with a pump system (Elveflow) consisting of AF1 OB1 controller and a MUX distributor. The time for new medium arrival was estimated by tubing volume and flow rate.

Microscopy

All time-lapse microscopic experiments were performed with a Nikon Ti-E inverted microscope equipped with a Nikon Perfect Focus System, an Andor iXon Ultra 897 EM-CCD, and a CoolLed pE2 or a Lumencor Aura II light excitation system. Bright field images were taken with a halogen lamp as the light

source, the light of which was passed through an ultraviolet light filter (420-nm beam-splitter). For NAD(P)H measurements, cells were excited with 365 nm (20% intensity, and 200 ms exposure), with a 350/50-nm band-pass filter, a 409-nm beam-splitter, and a 435/40-nm emission filter. For GFP measurements, cells were excited at 470 nm (20% intensity, 200 ms exposure) with a 470/40-nm band-pass filter, a 495-nm beam-splitter and a 525/50-nm emission filter. For mRFP measurements, cells were excited with 565 nm (20% intensity, 600 ms exposure) with a 560/40-nm band-pass filter, a 585-nm beam-splitter, and a 630/75-nm emission filter. Images were taken every 10 minutes for 0.025 gL^{-1} glucose condition, or every 5 minutes for 10 gL^{-1} glucose condition. For all sets of experiment, a 40x Nikon Super Fluor-Apochromat objective was used. NIS element software was used to control the microscope.

Analysis of Whi5 localization, budding and cytokinesis frequency

Cell cycle markers (Whi5 exiting the nucleus - START, budding - S phase, Whi5 entering the nucleus - mitotic exit, and cytokinesis) were analyzed for each experiment, using either brightfield images (budding and cytokinesis) or green fluorescence images (Whi5 localization). To determine the budding and cytokinesis frequency of randomly selected cells, we chose a time window of 300 minutes for the cells growing on steady-state high glucose or right after the nutrient shift from low to high glucose, whereas a 700 minutes window was used for cells growing on steady-state low glucose or after the shift from high to low glucose. These time frames reflect three times the average cell cycle duration on each nutrient condition.

Analysis of the metabolic frequency in Cdc14 depleted cells

To determine the metabolic oscillation frequency when mitotic exit is halted, we used data from a Cdc14 auxin degron depletion experiment (Papagiannakis et al., 2017a). We detrended the NAD(P)H data of each cell by dividing over a LOWESS spline fitted using the statsmodels package (Seabold et al., 2017) in Python. The detrended data was then shifted by subtracting 1 from each datapoint and we performed an autocorrelation analysis (correlating the detrended data with itself) using the correlate function from SciPy package Oliphant, 2007) in Python. A peak finding algorithm from the peakutils package (Negri and Vestri, 2017) in Python was used to determine the peak of autocorrelation function. The period (min) of each oscillation was determined by subtracting the peak indexes. We converted the period of the oscillations (min) to radial frequency (rad/h) by taking its reciprocal, multiplying it with 2π radians and converting minutes to hours. The frequency of oscillations before and after the Cdc14 depletion was used for analysis, while oscillations during the depletion process were discarded.

Cdc20 depletion and data analysis

To simultaneously perturb mitotic exit and S phase, we added a degron tag to the C-terminus of Cdc20 on its genomic loci. We created plasmids with Gibson DNA Assembly (New England Biolab) (Gibson et al., 2009) and inserted our genetic constructs into the yeast genome via homologous recombination (Gietz and Schiestl, 2007). To examine the dynamics of Cdc20 depletion (data not shown), we created plasmid G30 using the primers in Table S3. This genetic construct allowed us to tag Cdc20 with mCherry followed by the degron tag. We monitored genome replication using histone Hta2 fused to mRFP (C-terminal fusion). Thus, to combine genome measurements (Hta2-mRFP) and Cdc20 depletion we had to remove the mCherry tag from Cdc20. Specifically, we removed mCherry from the G30 plasmid using PCR followed by a second Gibson DNA Assembly reaction, to create plasmid G31. We used G31 to transform a *YSBN16 Whi5::Whi5-eGFP-HIS3MX6, HO::OsTIR1-KanMX4, Hta2::Hta2-mRFP1-Ble* strain, and selected with Nourseothricin (Werner BioAgents), obtaining the YSBN16 Cdc20-AID strain. Correct cassette integration was checked with PCR. For strains and primer sequences see Key Resources Table and Table S3. Full sequence of plasmids, DNA materials or strains are available on request.

To deplete Cdc20, the inflow of the microfluidic chip was switched from normal medium to medium with 0.1 mM of the synthetic auxin substitute 1-naphthalene-acetic acid (NAA) (Sigma Aldrich). A control strain with a green fluorescent protein fused to the degron tag was co-loaded onto the chip, to denote the exact timepoint of auxin-inducible protein depletion. Hyphal cells were segmented manually with ImageJ polygon selection tool (Schneider et al., 2012), while normally growing cells were segmented with the ImageJ plugin BudJ (Ferrezuelo et al., 2012), using the bright field channel, after which fluorescence values of each channel was background corrected and determined. NAD(P)H and GFP channels were background corrected with a rolling ball algorithm implemented in ImageJ before determining fluorescence. Hta2-mRFP fluorescence measurements of YSBN16 Cdc20-AID strain was background corrected by subtracting the mode value of segmented area. Genome copy number was estimated by the total amount of Hta2-mRFP fluorescence signal of the segmented cells (sum of background corrected pixel intensities), normalized by the lowest value measured during the corresponding G1 cell cycle phase (before cells started the DNA replication), which corresponds to one genome copy.

Directional statistics of phases of the cell cycle oscillators

For phase angles, the sample space is the unit circle. Thus, the standard methods of analyzing univariate measurement data cannot be used. Directional methods are required to take the structure of the sample space into account (Mardia and Jupp, 2000). Therefore, to obtain the correct mean and standard deviations of the phases of the cell cycle oscillators relative to the metabolism, we used directional statistics.

To calculate the mean of a given N number of angles (θ_i), first we considered the mean horizontal ($\bar{C}$) and vertical ($\bar{S}$) positions in cartesian coordinates described by these angles:

$$\bar{C} = \frac{1}{N}\sum_{i=1}^{N}\cos\theta_i \quad (3)$$

$$\bar{S} = \frac{1}{N}\sum_{i=1}^{N}\sin\theta_i \quad (4)$$

Quadrant-specific inverse tangent of the angle created by these two quantities (Eq. 3,4) results in the mean angle ($\bar{\theta}$) (Jammalamadaka and SenGupta, 2001):

$$\bar{\theta} = \begin{cases} \arctan\left(\frac{\bar{S}}{\bar{C}}\right) & if \quad \bar{C} > 0, \bar{S} \geq 0 \\ \pi/2 & if \quad \bar{C} = 0, \bar{S} > 0 \\ \arctan\left(\frac{\bar{S}}{\bar{C}}\right) + \pi & if \quad \bar{C} < 0 \\ \arctan\left(\frac{\bar{S}}{\bar{C}}\right) + 2\pi & if \quad \bar{C} \geq 0, \bar{S} < 0 \\ undefined & if \quad \bar{C} = 0, \bar{S} = 0 \end{cases} \quad (5)$$

We calculated this function (Eq. 5) by using "arctan2" (or "atan2") function (Oliphant, 2007). Using $\bar{S}$ and $\bar{C}$ again, we calculated the standard deviation (σ_θ) with

$$\bar{R} = \sqrt{\bar{C}^2 + \bar{S}^2} \quad (6)$$

$$\sigma_\theta = \sqrt{-2\ln(\bar{R})} \quad (7)$$

Estimation of the regularization parameter

To prevent over-fitting the data, we added a regularization term to the objective function, in which a regularization parameter (α) is multiplied with the sum of coupling constants (see main text Eq. 2). This is equivalent to L1 regularization (note that the coupling constants are non-negative), which is known to favor sparse solutions (Tibshirani, 1996). The addition of the regularization term forces as many coupling constants as possible to be zero, leading to topologies that can describe the experimental data with the fewest number of connections.

To determine the optimal value of the regularization parameter, we used the L-curve method, a graphical tool used to visualize the tradeoff between the magnitude of the regularization term and the quality of the fit (Hansen, 2001; Nasehi Tehrani et al., 2012). Here, as the regularization parameter increases, the norm (magnitude) of the penalized parameters (i.e. sum of coupling constants) can decrease up to a point without significantly affecting the fitting residuals (i.e. WSS). At high regularization parameters, however, the fit quickly worsens. The "knee" of the L-curve represents a good tradeoff between the amount of regularization and the fit quality.

To generate the L-curve, we performed parameter estimations using different regularization parameters in the range from 10^{-8} to 1000, sampled logarithmically. Each optimization run included 1000 multistart optimizations (using GAMS/CONOPT solver) (Drud, 1994). We selected the lowest residual (WSS) we obtained from these 1000 multistart optimizations, with its corresponding estimated parameter set. Then, we plotted the log of the residuals (WSS) against the log of the regularized parameter norms (sum of coupling constants) yielding the L-curve (see Fig. S2). Here, we selected the alpha value which is closest to the corner (or the "knee") that is formed by the curve.

Derivation of a constraint for estimating parameter sets that yield stable solutions

To understand whether the model with the identified parameters would yield stable solutions (i.e. constant phase differences with respect to time), first we investigated how it would respond when the phases are perturbed. Assume that the system has a synchronized solution where all phases increase at the same rate (ω_{comp}). Let us call this solution $\theta_i^*(t)$. If we perturb the system with a small amount $\Delta\theta^0$ then equations can be described as:

$$\theta_i(t) = \theta_i^*(t) + \Delta\theta_i(t) \tag{8}$$

$$\frac{d\theta_i}{dt} = \frac{d\left(\theta_i^*(t)+\Delta\theta_i(t)\right)}{dt} = \omega_i - \sum_{j=1}^{4} K_{j,i} \sin\left(\theta_i^*(t) + \Delta\theta_i(t) - \theta_i^*(t) - \Delta\theta_j(t)\right)$$

$$= \omega_i - \sum_{j=1}^{4} K_{j,i} \sin\left(\theta_i^*(t) - \theta_j^*(t)\right) - \left(\sum_{j=1}^{4} K_{j,i} \cos\left(\theta_i^*(t) - \theta_j^*(t)\right)\right)\Delta\theta_i(t) + \tag{9}$$

$$\sum_{j=1}^{4} \left(K_{j,i} \cos\left(\theta_i^*(t) - \theta_j^*(t)\right) \Delta\theta_j(t)\right)$$

Eq. 9 is derived from the multidimensional Taylor theorem. Here. the first two terms of the right-hand side of the equation are equal to ω_{comp} and they cancel out $\frac{d\theta_i^*(t)}{dt}$ term. The remainder of the equation is equal to $\frac{d(\Delta\theta(t))}{dt}$. Since the phase differences in cosine terms are constant and equal to the phase differences at the equilibrium solution, we finally get a linear equation for the deviation of each oscillator. This is described with

$$\frac{d(\Delta\theta(t))}{dt} = A\Delta\theta \tag{10}$$

The stability of the Kuramoto model that we defined can be estimated by the eigenvalues of the Jacobian matrix calculated at a certain state (i.e. set of phases). The elements of the Jacobian matrix ($\boldsymbol{A}$) have the following structure:

$$\begin{aligned} \boldsymbol{A}_{i,i} &= -\sum_{j=1}^{4} K_{j,i} \cos\left(\theta_i - \theta_j\right) \\ \boldsymbol{A}_{i,j} &= K_{j,i} \cos\left(\theta_i - \theta_j\right) \end{aligned} \tag{11}$$

It can be observed that the sum of each row of $\boldsymbol{A}$ is equal to zero which suggests that it is a singular matrix. Therefore, it has one zero eigenvalue corresponding to the eigenvector $\mathbf{1}$ (4-by-1 vector of ones). If the rest of the eigenvalues of A have negative real parts, the synchronized solution is locally asymptotically stable, meaning that if we introduce a small perturbation to the phases, the system will return to the original synchronized solution.

In order to obtain parameter sets which yield stable systems at the estimated phase differences, we embedded this property into the optimization problem as a nonlinear constraint. To do this, we used the Routh-Hurwitz stability criterion (Franklin et al., 1993). First, using a unitary transformation we created another matrix ($\boldsymbol{B}$), which has a submatrix with same non-zero eigenvalues as $\boldsymbol{A}$:

$$\boldsymbol{B} = \boldsymbol{S}^{\boldsymbol{T}}\boldsymbol{A}\boldsymbol{S} \tag{12}$$

$$\boldsymbol{B} = \begin{bmatrix} 0 & 0^{1\times 3} \\ 0^{3\times 1} & \boldsymbol{B_1^{3\times 3}} \end{bmatrix} \tag{13}$$

Here, $\boldsymbol{S}$ is an orthogonal matrix and all elements in its first column are 0.5 and the rest of the columns are unit vectors, which are mutually orthogonal and also orthogonal to $\mathbf{1}$. Since the structure of A is known, B can be calculated analytically given the transformation matrix S. The characteristic polynomial of the submatrix $\boldsymbol{B_1}$ is given by

$$p_{\boldsymbol{B_1}}(x) = \det\left(x\boldsymbol{I}_3 - \boldsymbol{B_1}\right) \tag{14}$$

where $\boldsymbol{I}_3$ is 3-by-3 identity matrix.

The Routh-Hurwitz criterion determines the condition under which the real parts of the roots of the characteristic polynomial of $\boldsymbol{B_1}$ (i.e. non-zero eigenvalues of $\boldsymbol{A}$) are negative and therefore the system is asymptotically stable. Given that B1 is a 3-by-3 matrix, its characteristic polynomial will have a degree of three. Writing this polynomial as

$$p_{\boldsymbol{B_1}}(x) = x^3 + b_2x^2 + b_1x + b_0 \tag{15}$$

the Routh-Hurwitz criterion implies that all its roots will have negative real parts if and only if

$$\begin{matrix} b_2,\, b_0 > 0 \\ b_2 b_1 > b_0 \end{matrix} \tag{16}$$

By solving Eq. 14, we calculated the coefficients of the characteristic polynomial in Eq. 15 as

$$\begin{matrix} b_0 = \boldsymbol{B_{1_{1,1}}B_{1_{2,3}}B_{1_{3,2}}} - \boldsymbol{B_{1_{1,1}}B_{1_{2,2}}B_{1_{3,3}}} + \boldsymbol{B_{1_{1,2}}B_{1_{2,1}}B_{1_{3,3}}} \\ - \boldsymbol{B_{1_{1,2}}B_{1_{2,3}}B_{1_{3,1}}} - \boldsymbol{B_{1_{1,3}}B_{1_{2,1}}B_{1_{3,2}}} + \boldsymbol{B_{1_{1,3}}B_{1_{2,2}}B_{1_{3,1}}} \end{matrix} \tag{17}$$

$$b_1 = \boldsymbol{B_{1_{1,1}}B_{1_{2,2}}} - \boldsymbol{B_{1_{1,2}}B_{1_{2,1}}} + \boldsymbol{B_{1_{1,1}}B_{1_{3,3}}} - \boldsymbol{B_{1_{1,3}}B_{1_{3,1}}} + \boldsymbol{B_{1_{2,2}}B_{1_{3,3}}} - \boldsymbol{B_{1_{2,3}}B_{1_{3,2}}} \tag{18}$$

$$b_2 = -\boldsymbol{B_{1_{1,1}}} - \boldsymbol{B_{1_{2,2}}} - \boldsymbol{B_{1_{3,3}}} \tag{19}$$

We introduced the constraint in Eq. 16 only in the fastest and slowest nutrient conditions (see Interaction topologies and natural frequencies estimated from experimental data). Therefore, the optimization problem we need to solve becomes

$$\underset{\widetilde{\omega}_{comp,c},\,\widetilde{\omega}_{MET,c},\,\tilde{\theta}_{i_c},\,K_{j,i},\,\omega_{i_{(i\neq MET)}}}{minimize} \sum_c \left(\frac{\omega^m_{comp,c}-\widetilde{\omega}_{comp,c}}{\sigma^m_{\omega_{comp,c}}}\right)^2 + \sum_c \left(\frac{\omega^m_{MET,c}-\widetilde{\omega}_{MET,c}}{\sigma^m_{\omega\ MET,c}}\right)^2$$

$$+ \sum_c \sum_{i,i\neq MET} \left(\frac{\theta^m_{i_c}-\tilde{\theta}_{i_c}}{\sigma^m_{\theta_{i_c}}}\right)^2 + \alpha \sum_{i,j\neq i} K_{j,i}$$

$$subject\ to$$

$$\widetilde{\omega}_{comp,c} = \widetilde{\omega}_{MET,c} - \sum_{j\neq MET} K_{j,MET}\sin\left(\tilde{\theta}_{MET_c} - \tilde{\theta}_{j_c}\right)$$

$$\widetilde{\omega}_{comp,c} = \omega_{i_{(i\neq MET)}} - \sum_{i\neq j, i\neq M} K_{j,i}\sin\left(\tilde{\theta}_{i_c} - \tilde{\theta}_{j_c}\right)$$

$$K_{j,i}, \omega_{i_{(i\neq MET)}} \geq 0 \qquad (20)$$

$$\boldsymbol{A}_{d_{i,i}} = -\sum_{j=1}^{4} K_{j,i}\cos\left(\tilde{\theta}_{i_d} - \tilde{\theta}_{j_d}\right)$$
$$\boldsymbol{A}_{d_{i,j}} = K_{j,i}\cos\left(\tilde{\theta}_{i_d} - \tilde{\theta}_{j_d}\right)$$

$$\boldsymbol{B_d} = \boldsymbol{S^T A_d S}$$

$$\boldsymbol{B}_{\mathbf{1}_{p,q}} = \boldsymbol{B}_{d_{i,j}} \ \forall\, \boldsymbol{i,j} \in \{\mathbf{2,3,4}\}\ \boldsymbol{and}\ \forall\, \boldsymbol{p,q} \in \{\mathbf{1,2,3}\}$$

$$b_{\mathrm{d}_0} = \boldsymbol{B}_{\mathbf{1}_{1,1}}\boldsymbol{B}_{\mathbf{1}_{2,3}}\boldsymbol{B}_{\mathbf{1}_{3,2}} - \boldsymbol{B}_{\mathbf{1}_{1,1}}\boldsymbol{B}_{\mathbf{1}_{2,2}}\boldsymbol{B}_{\mathbf{1}_{3,3}} + \boldsymbol{B}_{\mathbf{1}_{1,2}}\boldsymbol{B}_{\mathbf{1}_{2,1}}\boldsymbol{B}_{\mathbf{1}_{3,3}}$$
$$- \boldsymbol{B}_{\mathbf{1}_{1,2}}\boldsymbol{B}_{\mathbf{1}_{2,3}}\boldsymbol{B}_{\mathbf{1}_{3,1}} - \boldsymbol{B}_{\mathbf{1}_{1,3}}\boldsymbol{B}_{\mathbf{1}_{2,1}}\boldsymbol{B}_{\mathbf{1}_{3,2}} + \boldsymbol{B}_{\mathbf{1}_{1,3}}\boldsymbol{B}_{\mathbf{1}_{2,2}}\boldsymbol{B}_{\mathbf{1}_{3,1}}$$

$$b_{\mathrm{d}_1} = \boldsymbol{B}_{\mathbf{1}_{1,1}}\boldsymbol{B}_{\mathbf{1}_{2,2}} - \boldsymbol{B}_{\mathbf{1}_{1,2}}\boldsymbol{B}_{\mathbf{1}_{2,1}} + \boldsymbol{B}_{\mathbf{1}_{1,1}}\boldsymbol{B}_{\mathbf{1}_{3,3}} - \boldsymbol{B}_{\mathbf{1}_{1,3}}\boldsymbol{B}_{\mathbf{1}_{3,1}} + \boldsymbol{B}_{\mathbf{1}_{2,2}}\boldsymbol{B}_{\mathbf{1}_{3,3}} - \boldsymbol{B}_{\mathbf{1}_{2,3}}\boldsymbol{B}_{\mathbf{1}_{3,2}}$$

$$b_{\mathrm{d}_2} = -\boldsymbol{B}_{\mathbf{1}_{1,1}} - \boldsymbol{B}_{\mathbf{1}_{2,2}} - \boldsymbol{B}_{\mathbf{1}_{3,3}}$$

$$b_{\mathrm{d}_2}, b_{\mathrm{d}_0} > 0$$

$$b_{\mathrm{d}_2} b_{\mathrm{d}_1} > b_{\mathrm{d}_0}$$

Here, d denotes the fastest and the slowest growth conditions only (10 gL^{-1} glucose and 20 gL^{-1} pyruvate).

Simulations with dynamic perturbation of metabolic frequency and removal of cell cycle elements

To integrate the system of ODEs with the identified parameter sets, we used the ode15s solver in MATLAB. To simulate the nutrient shift conditions, we replaced the natural frequency of metabolism with the following time-dependent piecewise functions

683 $$\frac{d\theta_{MET}}{dt} = \omega_{MET}(t) - \sum_{j\neq i}^{N} K_{j,i} sin(\theta_i - \theta_j) \quad (21)$$

684 $$\omega_{MET}(t) = \begin{cases} \omega_{MET,1} & if\ t \leq t_1 \\ \omega_{MET,1} + (t - t_1)\ \frac{(\omega_{MET,2} - \omega_{MET,1})}{t_2 - t_1} & if\ t_1 < t < t_2 \\ \omega_{MET,2} & if\ t \geq t_2 \end{cases} \quad (22)$$

685 For the simulations where we shifted the natural metabolic frequency gradually, we used the piecewise
686 function in Eq. 22. On the other hand, for the simulations where we changed the metabolic frequency in a
687 stepwise manner, we used the following piecewise-constant function

688 $$\omega_{MET}(t) = \begin{cases} \omega_{MET,1}\ if\ t < t_s \\ \omega_{MET,2}\ if\ t \geq t_s \end{cases} \quad (23)$$

689 Here, $\omega_{MET}(t)$ is the time-dependent function, t_1 and t_2 are the time points where the gradual natural
690 metabolic frequency shift starts and stops respectively. t_s is the time point where the natural metabolic
691 frequency is switched in a stepwise manner. $\omega_{MET,1}$ and $\omega_{MET,2}$ are initial and final values for the natural
692 metabolic frequency respectively.

693 To simulate the system without mitotic exit, we made all the coupling constants from and to mitotic exit
694 equal to zero ($K_{i,M}, K_{M,i} = 0\ \forall\ i \in \{MET, START, S\}$). Also, to simulate the system without mitotic exit
695 and S, we set all coupling constants from and to mitotic exit and S equal to zero, leaving only $K_{START,MET}$
696 and $K_{MET,START}$ to be non-zero. We used the phases differences that we estimated at 10 gL^{-1} glucose
697 condition.

698 QUANTIFICATION AND STATISTICAL ANALYSIS

699 We specify the statistical tests used, the exact values of n, what n represents, and the dispersion and
700 precision measures in the respective figure legends.

701 DATA AND CODE AVAILABILITY

702 The code for the regression including the used experimental data (implemented in GAMS) and the
703 dynamics simulations of the coupled oscillator system (implemented in MATLAB) is available from the
704 lab's GitHub site: https://github.com/molecular-systems-biology.

705

Supplemental video

Movie S1: Cdc20 depletion leads to periodic biomass increase and halted genome replication, referring to Figure 6D-H.

Left: Green fluorescence images of several YSBN6.G2J cells (upper figure) and the mean green fluorescence intensity (GFP-AID) of 9 analyzed YSBN6.G2J cells (lower figure) show when the auxin-induced protein depletion got effective. Middle: Brightfield images (upper figure) and the perimeter/derivative of perimeter (lower figure) of the exemplary cell, shown in Figure 6E. Right: Red fluorescence images (upper figure) and genome copy number derived from the total amount of Hta2-mRFP fluorescence (lower figure) in the same cell. Static vertical line: time point where the GFP-AID protein, and presumably Cdc20-AID were depleted. Moving vertical line: denoting time steps as corresponding to the images. Exact time is shown in the upper-left corner. Scale bar: 10 μm.

References

Acebrón, J.A., Bonilla, L.L., Vicente, C.J.P., Ritort, F., and Spigler, R. (2005). The Kuramoto model: A simple paradigm for synchronization phenomena. Rev. Mod. Phys. *77*, 137–185.

Al-Feel, W., DeMar, J.C., and Wakil, S.J. (2003). A *Saccharomyces cerevisiae* mutant strain defective in acetyl-CoA carboxylase arrests at the G2/M phase of the cell cycle. Proc. Natl. Acad. Sci. U. S. A. *100*, 3095–3100.

Alderisio, F., Fiore, G., and di Bernardo, M. (2017). Reconstructing the structure of directed and weighted networks of nonlinear oscillators. Phys. Rev. E *95*, 042302.

Arenas, A., Díaz-Guilera, A., Kurths, J., Moreno, Y., and Zhou, C. (2008). Synchronization in complex networks. Phys. Rep. *469*, 93–153.

Ball, D.A., Marchand, J., Poulet, M., Baumann, W.T., Chen, K.C., Tyson, J.J., and Peccoud, J. (2011). Oscillatory dynamics of cell cycle proteins in single yeast cells analyzed by imaging cytometry. PLoS One *6*, e26272.

Bardwell, L. (2004). A walk-through of the yeast mating pheromone response pathway. Peptides *25*, 1465–1476.

Barik, D., Baumann, W.T., Paul, M.R., Novak, B., and Tyson, J.J. (2010). A model of yeast cell-cycle regulation based on multisite phosphorylation. Mol. Syst. Biol. *6*, 405.

Baumgartner, B.L., O'Laughlin, R., Jin, M., Tsimring, L.S., Hao, N., and Hasty, J. (2018). Flavin-based metabolic cycles are integral features of growth and division in single yeast cells. Sci. Rep. *8*, 1–10.

Blanter, E., Le Mouël, J.L., Shnirman, M., and Courtillot, V. (2016). Kuramoto Model with Non-symmetric Coupling Reconstructs Variations of the Solar-Cycle Period. Sol. Phys. *291*, 1003–1023.

Bloom, J., and Cross, F.R. (2007). Multiple levels of cyclin specificity in cell-cycle control. Nat. Rev. Mol. Cell Biol. *8*, 149–160.

Burnetti, A.J., Aydin, M., and Buchler, N.E. (2016). Cell cycle Start is coupled to entry into the yeast metabolic cycle across diverse strains and growth rates. Mol. Biol. Cell *27*, 64–74.

Cadieu, C.F., and Koepsell, K. (2010). Phase coupling estimation from multivariate phase statistics. Neural Comput. *22*, 3107–3126.

Cai, L., Sutter, B.M., Li, B., and Tu, B.P. (2011). Acetyl-CoA Induces Cell Growth and Proliferation by Promoting the Acetylation of Histones at Growth Genes. Mol. Cell *42*, 426–437.

Cho, C., Motta, F.C., Kelliher, C.M., Deckard, A., Haase, S.B., Motta, F.C., Kelliher, C.M., and Deckard, A. (2017). Reconciling conflicting models for global control of cell-cycle transcription. Cell Cycle *16*, 1965–1978.

Costanzo, M., Nishikawa, J.L., Tang, X., Millman, J.S., Schub, O., Breitkreuz, K., Dewar, D., Rupes, I., Andrews, B., and Tyers, M. (2004). CDK Activity Antagonizes Whi5, an Inhibitor of G1/S Transcription in Yeast. Cell *117*, 899–913.

Coudreuse, D., and Nurse, P. (2010). Driving the cell cycle with a minimal CDK control network. Nature *468*, 1074–1079.

Cvrcková, F., and Nasmyth, K. (1993). Yeast G1 cyclins CLN1 and CLN2 and a GAP-like protein have a role in bud formation. EMBO J. *12*, 5277–5286.

Dörfler, F., and Bullo, F. (2011). On the Critical Coupling for Kuramoto Oscillators. SIAM J. Appl. Dyn. Syst. *10*, 1070–1099.

Drud, A.S. (1994). CONOPT—A Large-Scale GRG Code. ORSA J. Comput. *6*, 207–216.

Ferrezuelo, F., Colomina, N., Palmisano, A., Garí, E., Gallego, C., Csikász-Nagy, A., and Aldea, M. (2012). The critical size is set at a single-cell level by growth rate to attain homeostasis and adaptation. Nat. Commun. *3*, 1012.

Franklin, G.F., Powell, J.D., and Emami-Naeini, A. (1993). Feedback control of dynamic systems (Addison-Wesley Longman Publishing Co., Inc.).

Gibson, D.G., Young, L., Chuang, R.-Y., Venter, J.C., Hutchison, C.A., and Smith, H.O. (2009). Enzymatic assembly of DNA molecules up to several hundred kilobases. Nat. Methods *6*, 343–345.

Gietz, R.D., and Schiestl, R.H. (2007). High-efficiency yeast transformation using the LiAc/SS carrier DNA/PEG method. Nat. Protoc. *2*, 31–34.

Hansen, P.C. (2001). The L-curve and its use in the numerical treatment of inverse problems. In: Computational Inverse Problems in Electrocardiology, ed. by P. Johnston, WIT Press, 119–142.

Hong, H., O'Keeffe, K.P., and Strogatz, S.H. (2016). Correlated disorder in the Kuramoto model: Effects on phase coherence, finite-size scaling, and dynamic fluctuations. Chaos An Interdiscip. J. Nonlinear Sci. *26*, 103105.

Huberts, D.H.E.W., Sik Lee, S., Gonzáles, J., Janssens, G.E., Vizcarra, I.A., and Heinemann, M. (2013). Construction and use of a microfluidic dissection platform for long-term imaging of cellular processes in budding yeast. Nat. Protoc. *8*, 1019–1027.

Jammalamadaka, S.R., and SenGupta, A. (2001). Topics in Circular Statistics (WORLD SCIENTIFIC).

Kralemann, B., Pikovsky, A., and Rosenblum, M. (2011). Reconstructing phase dynamics of oscillator networks. Chaos An Interdiscip. J. Nonlinear Sci. *21*, 025104.

Krylov, D.M., Nasmyth, K., and Koonin, E. V. (2003). Evolution of Eukaryotic Cell Cycle Regulation. Curr. Biol. *13*, 173–177.

Kuramoto, Y. (1984). Chemical Oscillations, Waves, and Turbulence (Berlin, Heidelberg: Springer Berlin Heidelberg).

Litsios A, Huberts DHEW, Terpstra H, Guerra P, Schmidt A, Buczak K, Papagiannakis A, Rovetta M, Hekelaar J, Hubmann G, Exterkate M, Milias-Argeitis A, Heinemann M (2019). Differential scaling between G1 protein production and cell size dynamics promotes commitment to the cell division cycle in budding yeast. Nat. Cell. Biol., accepted. <we will provide you with the DOI during the proofing stage>

Liu, X., Wang, X., Yang, X., Liu, S., Jiang, L., Qu, Y., Hu, L., Ouyang, Q., and Tang, C. (2015). Reliable cell cycle commitment in budding yeast is ensured by signal integration. Elife *4*. 10.7554/eLife.03977.

Lu, Y., and Cross, F.R. (2010). Periodic cyclin-cdk activity entrains an autonomous cdc14 release oscillator. Cell *141*, 268–279.

Mardia, K. V, and Jupp, P. (2000). Directional Statisitics (JOHN WILEY & SONS).

Morawska, M., and Ulrich, H.D. (2013). An expanded tool kit for the auxin-inducible degron system in budding yeast. Yeast *30*, 341–351.

Münzner, U., Klipp, E., and Krantz, M. (2019). A comprehensive, mechanistically detailed, and executable model of the cell division cycle in Saccharomyces cerevisiae. Nat. Commun. *10*, 1308.

Nasehi Tehrani, J., McEwan, A., Jin, C., and van Schaik, A. (2012). L1 regularization method in electrical impedance tomography by using the L1-curve (Pareto frontier curve). Appl. Math. Model. *36*, 1095–1105.

Negri, L.H., and Vestri, C. (2017). lucashn/peakutils: v1.3.0 (Zenodo).

Nishimura, K., Fukagawa, T., Takisawa, H., Kakimoto, T., and Kanemaki, M. (2009). An auxin-based degron system for the rapid depletion of proteins in nonplant cells. Nat. Methods *6*, 917–922.

Oliphant, T.E. (2007). Python for Scientific Computing. Comput. Sci. Eng. *9*, 10–20.

Orlando, D.A., Lin, C.Y., Bernard, A., Wang, J.Y., Socolar, J.E.S., Iversen, E.S., Hartemink, A.J., and Haase, S.B. (2008). Global control of cell-cycle transcription by coupled CDK and network oscillators. Nature *453*, 944–947.

Papagiannakis, A., Niebel, B., Wit, E.C., and Heinemann, M. (2017a). Autonomous Metabolic Oscillations Robustly Gate the Early and Late Cell Cycle. Mol. Cell *65*, 285–295.

Papagiannakis, A., de Jonge, J.J., Zhang, Z., and Heinemann, M. (2017b). Quantitative characterization of the auxin-inducible degron: a guide for dynamic protein depletion in single yeast cells. Sci. Rep. *7*, 4704.

Pitt, J.A., and Banga, J.R. (2019). Parameter estimation in models of biological oscillators: an automated regularised estimation approach. BMC Bioinformatics *20*, 82.

Polymenis, M., and Aramayo, R. (2015). Translate to divide: control of the cell cycle by protein synthesis. Microb. Cell *2*, 94–104.

Rahi, S.J., Pecani, K., Ondracka, A., Oikonomou, C., and Cross, F.R. (2016). The CDK-APC/C Oscillator Predominantly Entrains Periodic Cell-Cycle Transcription. Cell *165*, 475–487.

Scaglia, N., Tyekucheva, S., Zadra, G., Photopoulos, C., and Loda, M. (2014). De novo fatty acid synthesis at the mitotic exit is required to complete cellular division. Cell Cycle *13*, 859–868.

Schmoller, K.M., Turner, J.J., Kõivomägi, M., and Skotheim, J.M. (2015). Dilution of the cell cycle inhibitor Whi5 controls budding-yeast cell size. Nature *526*, 268–272.

Schneider, C.A., Rasband, W.S., and Eliceiri, K.W. (2012). NIH Image to ImageJ: 25 years of image analysis. Nat. Methods *9*, 671–675.

Schwob, E., and Nasmyth, K. (1993). CLB5 and CLB6, a new pair of B cyclins involced in S phase and and mitotic spindle formation in S. cerevisiae. Genes Dev. *7*, 1160–1175.

827 Seabold, S., Perktold, J., ChadFulton, Shedden, K., j-grana6, Arel-Bundock, V., McKinney, W.,
828 Langmore, I., Baker, B., Gommers, R., et al. (2017). statsmodels/statsmodels: Version 0.9.0 Release
829 (Zenodo).

830 Sherr, C.J. (2004). Living with or without cyclins and cyclin-dependent kinases. Genes Dev. *18*, 2699–
831 2711.

832 Shi, L., and Tu, B.P. (2013). Acetyl-CoA induces transcription of the key G1 cyclin CLN3 to promote
833 entry into the cell division cycle in Saccharomyces cerevisiae. Proc. Natl. Acad. Sci. *110*, 7318–7323.

834 Shirayama, M., Zachariae, W., Ciosk, R., and Nasmyth, K. (1998). The Polo-like kinase Cdc5p and the
835 WD-repeat protein Cdc20p/fizzy are regulators and substrates of the anaphase promoting complex in
836 Saccharomyces cerevisiae. EMBO J. *17*, 1336–1349.

837 Shirayama, M., Tóth, A., Gálová, M., and Nasmyth, K. (1999). APC(Cdc20) promotes exit from mitosis
838 by destroying the anaphase inhibitor Pds1 and cyclin Clb5. Nature *402*, 203–207.

839 Slavov, N., Macinskas, J., Caudy, A., and Botstein, D. (2011). Metabolic cycling without cell division
840 cycling in respiring yeast. Proc. Natl. Acad. Sci. *108*, 19090–19095.

841 Strogatz, S.H. (2000). From Kuramoto to Crawford: exploring the onset of synchronization in populations
842 of coupled oscillators. Phys. D Nonlinear Phenom. *143*, 1–20.

843 Tibshirani, R. (1996). Regression Shrinkage and Selection via the Lasso. J. R. Stat. Soc. Ser. B Stat.
844 Methodol. *58*, 267–288.

845 Timme, M. (2007). Revealing network connectivity from response dynamics. Phys. Rev. Lett. *98*, 1–4.

846 Tirabassi, G., Sevilla-Escoboza, R., Buldú, J.M., and Masoller, C. (2015). Inferring the connectivity of
847 coupled oscillators from time-series statistical similarity analysis. Sci. Rep. *5*, 1–14.

848 Tyson, J.J., and Novak, B. (2008). Temporal Organization of the Cell Cycle. Curr. Biol. *18*, 759–768.

849 Villaverde, A.F., and Banga, J.R. (2017). Dynamical compensation and structural identifiability of
850 biological models: Analysis, implications, and reconciliation. PLOS Comput. Biol. *13*, e1005878.

851 Wäsch, R., and Cross, F.R. (2002). APC-dependent proteolysis of the mitotic cyclin Clb2 is essential for
852 mitotic exit. Nature *418*, 556–562.

853 Zach, R., Grallert, B., Převorovský, M., Tvarůžková, J., Schätz, M., and Ťupa, O. (2018). Mitotic defects
854 in fission yeast lipid metabolism 'cut' mutants are suppressed by ammonium chloride. FEMS Yeast Res.
855 *18*, 1–7.

856